Response of water vapour D-excess to land-atmosphere interactions in a semi-arid environment

Stephen D. Parkes[1], Matthew F. McCabe[1,2], Alan D. Griffiths[3], Lixin Wang[4], Scott Chambers[3],

Ali Ershadi[1,2], Alastair G. Williams[3], Josiah Strauss[2], Adrian Element[3]

[1] Water Desalination and Reuse Centre, King Abdullah University of Science and Technology (KAUST), Jeddah, Saudi Arabia

[2] Department of Civil and Environmental Engineering, University of New South Wales, Sydney, Australia

[3] Australian Nuclear Science and Technology Organization, Sydney, New South Wales, Australia

[4] Department of Earth Sciences, Indiana University–Purdue University Indianapolis (IUPUI), Indianapolis

Corresponding Author: Stephen Parkes, stephen.parkes@kaust.edu.sa

20   Key points:

- Examine the influence of local land-atmosphere coupling on water vapour isotopes
- Diurnal cycle of D-excess in water vapour is determined by an interplay between large scale moisture sources and nocturnal processes
- The D-excess of the evaporation fluxes impose negative forcing on the ambient vapour
- Nocturnal D-excess values are determined by surface exchange and turbulent mixing

Abstract

The stable isotopic composition of water vapour provides information about moisture sources and processes difficult to obtain with traditional measurement techniques. Recently, it has been proposed that the D-excess ($d_v = \delta^2H - 8 \times \delta^{18}O$) of water vapour can provide a diagnostic tracer of continental moisture recycling. However, D-excess exhibits a diurnal cycle that has been observed across a variety of ecosystems and may be influenced by a range of processes beyond regional scale moisture recycling, including local evaporation (ET) fluxes. There is a lack of measurements of D-excess in evaporation (ET) fluxes, which has made it difficult to assess how ET fluxes modify the D-excess in water vapour (d_v). With this in mind, we employed a chamber based approach to directly measure D-excess in ET (d_{ET}) fluxes. We show that ET fluxes imposed a negative forcing on the ambient vapour and could not explain the higher daytime d_v values. The low d_{ET} observed here was sourced from a soil water pool that had undergone an extended drying period, leading to low D-excess in the soil moisture pool. A strong correlation between daytime d_v and locally measured relative humidity was consistent with an oceanic moisture source, suggesting that remote hydrological processes were the major contributor to daytime d_v variability. During the early evening, ET fluxes into a shallow nocturnal inversion layer caused a lowering of d_v values

42   near the surface. In addition, transient mixing of vapour with a higher D-excess from above the

43   nocturnal inversion modified these values, causing large within night variability. These results

44   indicate d_{ET} can generally be expected to show large spatial and temporal variability and to depend

45   on the soil moisture state. For long periods between rain events, common in semi-arid

46   environments, ET would be expected to impose negative forcing on the surface d_v. Spatial and

47   temporal variability of D-excess in ET fluxes therefore needs to be considered when using dv to

48   study moisture recycling and during extended dry periods with weak moisture recycling may act

49   as a tracer of the relative humidity at the oceanic moisture source.

50

1   Introduction

52   Climate change has the potential to significantly impact surface and atmospheric water budgets.

53   Our best understanding of future exchanges between the atmospheric water cycle and the land

54   surface on a regional to global scale, is likely to be gained through analysis of numerical

55   simulations (Decker et al. 2015; Evans and McCabe, 2010; Harding and Snyder, 2012; Wei et al.

56   2012). Consequently, continual improvement of available models is essential, but is contingent

57   upon ongoing validation and evaluation of model performance over a broad range of landscapes

58   and climate types (McCabe et al., 2016). To do this effectively, a diversity of datasets that directly

59   quantify processes represented within these models are required (McCabe et al., 2005).

60   Unfortunately, datasets that directly measure land-atmosphere exchange at the process level are

61   limited (Jana et al., 2016).

62 Water is composed of a number of stable isotopologues that have sufficient abundance to be

63 measured in atmospheric water vapour ($^1H_2^{16}O$, $^1H^2H^{16}O$, $^1H_2^{18}O$ and $^1H_2^{17}O$). The deviation of

64 the isotope ratios, reported as

65 $\delta = \left[\dfrac{R_{sample}}{R_{VSMOW}} - 1\right]$‰   (1)

66   where R is the isotope ratio ($^2H/^1H$ or $^{18}O/^{16}O$) and VSMOW (Vienna Standard Mean

67 Ocean Water), is the international standard for reporting water isotope ratios, and have potential

68 to evaluate land-atmosphere exchange by discriminating processes based on their isotopic

69 signature (Berkelhammer et al. 2013; Lee et al. 2009; Noone et al. 2013; Risi et al. 2013). Isotopic

70 ratios of water vapour (δ^2H and $\delta^{18}O$) can therefore provide information that is complimentary or

71 even unobtainable when using conventional measurement techniques.

72 The utility of water isotope ratios for tracing sources of moisture derives from the characteristic

73 equilibrium and kinetic isotopic fractionation that occurs when water undergoes a phase change,

74 causing light water molecules to preferentially accumulate in the vapour phase. Soil moisture is

75 typically enriched in heavy isotopes relative to the ocean (Gat, 1996), so water vapour derived

76 from land surface evaporation is expected to have a different isotopic composition to moisture

77 evaporated from the ocean. This has led to a number of studies using stable isotopes in precipitation

78 to partition oceanic and land derived sources (Froehlich et al. 2008; Tian et al. 2001). However,

79 land-atmosphere exchange is not restricted to periods of precipitation, and there are relatively few

80 studies examining the role of land-atmosphere exchange on ambient humidity budgets using stable

81 isotope observations of vapour (e.g. Aemisegger et al. 2014; Risi et al. 2013).

82 In addition to the source of moisture, the magnitude of isotopic fractionation that occurs when

83 water evaporates is related to the liquid surface temperature and humidity gradient between the

84 evaporating surface and atmosphere (Craig and Gordon, 1965). The temperature dependent

85 equilibrium exchange between liquid and vapour is the largest contributor to isotopic fractionation

86 during evaporation, with the fractionation for δ^2H approximately a factor of 8 greater than $\delta^{18}O$.

87 The effect of kinetic fractionation associated with moisture diffusing from the thin laminar layer

88 of vapour in equilibrium with the water surface to the turbulent atmosphere above is influenced by

89 the relative humidity of the atmosphere and wind speed (Merlivat and Jouzel, 1979). The kinetic

90 fractionation factors for δ^2H and $\delta^{18}O$ are similar, causing the ratio of δ^2H to $\delta^{18}O$ in the

91 evaporating vapour to decrease as kinetic effects increase with decreasing relative humidity. This

92 phenomenon has been observed for evaporative conditions over the Mediterranean sea (Gat et al.

93 2003; Pfahl and Wernli, 2009) and the Great Lakes in Northern USA (Gat et al. 1994; Vallet-

94 Coulomb et al. 2008).

95 The D-excess parameter (D-excess = $\delta^2H - 8 \times \delta^{18}O$) (Dansgaard, 1964), quantifies the non-

96 equilibrium isotopic fractionation. A reproducible relationship between the D-excess and relative

97 humidity near the ocean surface has been observed across a wide range of locations (Kurita, 2011;

98 Pfahl and Wernli, 2008; Steen-Larsen et al. 2015; Uemura et al. 2008). Therefore, it has been

99 suggested that for precipitation, D-excess is a good tracer of sea surface evaporative conditions

100 (Masson-Delmotte et al. 2005; Merlivat and Jouzel, 1979). However, this view has recently been

101 challenged due to the role local and regional scale land-atmosphere coupling has in modifying the

102 D-excess of atmospheric humidity over diurnal (Lai and Ehleringer, 2011; Simonin et al. 2014;

103 Welp et al. 2012; Zhao et al. 2014) and synoptic timescales (Aemisegger et al. 2014). As evidence

104   for the role ET plays in modifying the D-excess of water vapour (d_v), a diurnal cycle of d_v near the

105   land surface across a range of land surface types has been observed (Berkelhammer et al. 2013;

106   Simonin et al. 2014; Welp et al. 2012). The diurnal cycle shows higher values in the day, which

107   has been proposed to be driven by entrainment (Lai and Ehleringer, 2011; Welp et al. 2012), local

108   evapotranspiration sources (Simonin et al. 2014; Zhao et al. 2014) and meteorological conditions

109   affecting the D-excess of the evaporative fluxes (d_{ET}) (Welp et al. 2012; Zhao et al. 2014), coupled

110   with low nocturnal values resulting from equilibrium exchange between liquid and vapour pools

111   (Simonin et al. 2014) and dew fall (Berkelhammer et al. 2013). For synoptic scales, Aemisegger

112   *et al.* (2014) showed that moisture recycling from the land surface had a significant impact on d_v

113   for *in-situ* measurements in Switzerland. These studies have largely relied on isotopic models to

114   assess the contribution of ET fluxes, but a lack of d_{ET} measurements make it difficult to draw

115   robust conclusions.

116   The evidence provided by these studies suggest d_v is a tracer of moisture recycling both on diurnal

117   and synoptic time scales, and is influenced by dynamics of surface moisture budgets in the

118   atmospheric boundary layer (ABL). However, as noted by Welp *et al.* (2012), ET and entrainment

119   fluxes both increase as the ABL grows through the previous days residual layer, which can make

120   interpreting the role of local moisture recycling on d_v difficult. To overcome this, Simonin *et al.*

121   (2014) used a trajectory model to simulate the D-excess of vapour evaporated over the ocean. As

122   the d_v was greater than the modelled oceanic moisture source, it was assumed that high daytime

123   values were supported by local ET fluxes. Zhao *et al.* (2014) suggested that since, on cloudy days,

124   no diurnal cycle was observed for the d_v, that ET fluxes played a dominant role. Whilst these

125   studies provide compelling evidence for the role of ET driving the diurnal cycle of d_v, no

126   measurements of d_{ET} were made. To date the only measurements of d_{ET} have been presented by

127   Huang *et al.* (2014) over a maize crop in north west China. Interestingly, their direct measurements

128   conflicted with previous interpretations and showed that the d_{ET} invoked a negative forcing on d_v,

129   even though a strong diurnal cycle of high values in the day and low values at night were observed.

130   In order to better interpret the role of local moisture recycling on the diurnal cycle of d_v,

131   measurements of d_{ET} are required to assess if the negative forcing is consistent in different

132   ecosystems.

133   The aim of this work is to provide much needed d_{ET} measurements to investigate how ET fluxes

134   modulate the d_v diurnal cycle. To do this, chamber based measurements of the ET flux isotopic

135   compositions were combined with *in-situ* measurements of water vapour isotope ratios,

136   meteorological and radon concentration observations. The data was collected in a region of the

137   semi-arid Murray Darling basin in south-eastern Australia. These data represent the first such

138   collection of the δ^2H, δ^{18}O and D-excess in water vapour from this region of Australia. The

139   augmentation of the chamber based measurements with in-situ observations provide a framework

140   to directly assess the role local ET fluxes have on ambient vapour D-excess.

141   **2   Methods**

142   **2.1   Site Description**

143   During the austral autumn of 2011, a field campaign covering the period April 27 to May 11 was

144   conducted at the Baldry Hydrological Observatory (BHO) (-32.87, 148.54, 460 m above sea level)

145   located in the central-west of New South Wales, Australia (Figure 1). The climate of the region is

146   characterised as semi-arid with no clear wet season, a mean annual rainfall of 600 mm, and a mean

147   annual temperature of 24.2ºC (source Australian Bureau of Meteorology, 2015,

148   ). The BHO grassland eddy covariance flux tower was the central site of

149   measurements and was located in a natural grassland paddock of dimensions approximately 900m

150   (north-south) by 300m (west-east), with a gentle slope decreasing in elevation by approximately

151   20 m from southeast to northwest. The flux tower was located 650 m from the road to the south

152   and 200 m from a reforested paddock to the west. The forest site to the west and southwest was

153   reforested in 2001 with *Eucalyptus camaldulensis*, *Eucalyptus crebra* and *Corymbia maculate*. At

154   the time of the campaign these trees were approximately 10 m tall. All other adjacent paddocks

155   and most of the surrounding region had similar surface characteristics to the grassland

156   measurement site.

157   **2.2   Water stable isotope analyses**

158   **2.2.1   *In-situ* water vapour calibration and sampling**

159   In-situ water vapour isotope ratios were monitored using a Wavelength Scanning Cavity Ring

160   Down Spectrometer (WS-CRDS L115-I, Picarro Inc., Sunnyvale, CA, USA), while flux chambers

161   were interfaced to an Off Axis Integrated Cavity Output Spectrometer (OA-ICOS, DLT100, Los

162   Gatos Research (LGR), Mountain View, CA, USA) to determine the isotopic composition of ET

163   fluxes. Using an automated continuous flow calibration system (built in-house), we simultaneously

164   determined calibration coefficients for both analysers. Calibration experiments were designed to

165   determine the water vapour mixing ratio cross-sensitivity of isotope ratios and linearity of the δ^2H

166   and $\delta^{18}O$ measurements. More details on the calibration procedure are found in the supplementary

167   materials. Due to logistical constraints, the calibration system was not transported into the field,

168   so corrections were determined by compositing multiple calibration experiments run before and

169   after the campaign.

170   During the campaign, a secondary portable calibration system was employed to monitor time

171   dependent drift of the Picarro analyser (CTC HTC-Pal liquid autosampler; LEAP Technologies,

172   Carrboro, NC, USA). Two standards spanning expected water vapour δ^2H (-49.1 and -221.9‰)

173   and $\delta^{18}O$ (-9.17 and -27.57‰) ranges were injected at approximately 18 mmol.mol^{-1} on three

174   occasions during the campaign.

175   The uncertainty of measurements from both isotopic analysers was estimated by applying mixing

176   ratio cross-sensitivity and linearity corrections to all calibration measurements collected prior,

177   during and after the campaign. For the Picarro instrument, measurement uncertainty was 0.8, 0.2

178   and 1.9‰ for δ^2H_v, $\delta^{18}O_v$ and d_v, respectively. No calibrations were performed for the LGR in

179   field, so the measurement uncertainty was estimated by compositing calibration measurements

180   made before and after the campaign, which were 0.9, 0.4 and 3.3‰ for δ^2H, $\delta^{18}O$ and d_v.

181   Although no calibration experiments were run on the LGR during the campaign, simultaneous *in-*

182   *situ* measurements were made with the Picarro when chamber measurements were not operated.

183   During the day, average differences were -0.06 (±2.0), 0.13 (±0.5) and 0.4 (±3.3)‰ for δ^2H, $\delta^{18}O$

184   and d_v, respectively. A comparison of the analysers is shown in figure S1. At night, while the

185   Picarro was able to maintain a steady cavity and optical housing temperature, the LGR cavity

186   temperature dropped by up to 8°C. In response to the drop in cavity temperature, night time LGR

187   measurements of $\delta^{18}O$ and d_v and to a lesser extent the δ^2H, were physically unrealistic and

188   discarded from subsequent analyses. Chamber measurements were therefore restricted to between

189   09:00 (when the LGR cavity temperature had stabilised and *in-situ* measurements were again in

190   agreement with the Picarro) and 17:00 (before LGR cavity temperatures began dropping).

191   A schematic diagram illustrating the sampling design for water vapour is shown in Figure 2. Half-

192   hourly vertical profiles of humidity and isotopes were sampled by drawing air to the *in-situ*

193   analyser through 10 mm O.D. PTFE tubing, located at 5 heights on a 7.5 m tower (0.5, 1, 2, 5 and

194   7.5 m Above Ground Level). The instrument was interfaced to a 5 inlet manifold that enabled

195   sequential sampling of the different heights. Approximately 20 m of tubing was required to connect

196   the tower inlet to the analyser. A vacuum pump (MV 2 NT, Vacuubrand, Wertheim, Germany)

197   was used to draw air through all inlets to the analyser at a flow rate of 10 l.min^{-1}, with the Picarro

198   bleeding off the 0.03 l.min^{-1} through its measurement cavity. To avoid condensation, sample tubes

199   and intakes were wrapped in 15 W m^{-1} heat tape, insulated by Thermobreak pipe and placed inside

200   100 mm PVC pipe. The sample tube temperature was controlled using a Resistance Thermometer

201   Detector (RTD) coupled to a CAL3300 temperature controller (CAL controls Ltd., Grayslake, IL,

202   USA). The inlets at each height were constructed from inverted funnels with mesh filters. In this

203   study we present block hourly averages of all measurements collected at all heights.

204   **2.2.2   Flux chambers**

205   To separate the isotopic signatures of the ET flux components, flux chambers were deployed on

206   both bare soil and vegetated plots to determine the isotopic signature of the evaporative fluxes. An

207   open chamber was designed with a high volume to footprint ratio to avoid the chamber mixing

208   ratio rapidly reaching the dew point temperature (causing condensation) and to minimise impacts

209   on the evaporation environment. A schematic of the chamber design is shown in Figure 3. Four

210   flanged metal collars were inserted ~10 cm into the soil column two days before the beginning of

211   the campaign. While this was a short settling time for chamber bases, shallow roots of grass cover

212   within the chamber were largely unaffected. All vegetation was removed from bare soil plots when

213   the metal collars were inserted into the soil. A single chamber cover was constructed of 4 mm G-

214   UVT Plexiglass (Image Plastics, Padstow, Australia), selected for its higher transmittance of UV

215   and blue light. The dimensions of the chamber were 0.1 x 0.1 x 0.8 m (width x length x height),

216   with the inlets and outlets at 0.1 and 0.7 m above the surface, respectively. All sampling tube was

217   10 mm PTFE. The inlet to the chamber was connected to tubing that drew in air from 1.5 m above

218   the ground surface. The outlet was connected to a flowmeter (VFA-25, Dwyers, Michigan City,

219   IN, USA) that regulated the air flow at 10 l.min^{-1} and was driven by a two-stage diaphragm pump.

220   A T-piece was connected to the LGR, which bled off approximately 0.8 l.min^{-1}. All tubing between

221   chamber and the analyser were wrapped in heating tape (15 W m^{-2}) and foam insulation. High flow

222   rates were used to combat memory effects modifying the isotopic composition of the vapour within

223   the chamber. Analysis of chamber measurements were conducted on 2-5 minutes of data, so 2.5-

224   6.25 chamber volumes were exchanged.

225   To monitor the internal chamber environment, an air temperature and humidity probe (HMP155,

226   Vaisala, Vantaa, Finland) was mounted inside the chamber. To monitor the attenuation of the

227   incoming radiation by the chamber, photosynthetic flux density was measured (LI-190R, Licor,

228   Lincoln, NE, USA) inside and outside the chamber. Ten second averages of the temperature,

229   relative humidity and photosynthetic flux density were stored in a datalogger (CR1000, Campbell

230   Scientific, Logan, UT, USA). In the supplementary section we use these ancillary measurements

231   to assess the impact of observed changes in chamber environment on the isotopic composition of

232   the ET flux. The largest contributor to uncertainty caused by changing the evaporative

233   environment was the temperature, although these affects were small compared to the overall

234   variability of the chamber derived ET isotopic compositions.

2.2.3 Isotopic composition of ET flux from chamber measurements

Mass balance or Keeling mixing (Keeling, 1958; Wang et al. 2013) models have been applied to determine the isotopic composition of ET fluxes from chamber measurements (Lu et al., 2016; Wang et al., 2013b). The focus of this work was not to evaluate chamber measurement techniques. Considering that it has been shown that Keeling and mass balance methods give very similar results (Lu et al., 2016; Wang et al., 2013b) we focus on using the Keeling mixing model, given by

$$\delta_{chamber} = q_{BG} \frac{(\delta_{BG} - \delta_{ET})}{q_{chamber}} + \delta_{ET} \qquad\qquad (2)$$

where q_{BG} is the water vapour mixing ratio entering the chamber through the inlet and δ_{BG} its isotopic composition, $q_{chamber}$ is the mixing ratio in the chamber and δ_{ET} is the isotopic composition of the ET flux. The δ_{ET} is determined from the intercept of $\delta_{chamber}$ against $1/q_{chamber}$. A key assumption of the Keeling method is that the isotopic composition of the background vapour and the evaporation flux remain constant during the chamber measurements. For chamber measurements longer than 5 minutes, non-linear Keeling plots were commonly observed, indicating a change in isotopic composition of one of the sources of vapour. We therefore restricted the Keeling analysis to a maximum of 5 minutes after an increase in the concentration was observed by the analyser. Ensuring the linearity of Keeling plots also ensured that the influence of memory effects was minimised. Memory effects would constitute an additional moisture source, violating the two source assumption of the Keeling methods and reducing Keeling plot linearity. The analysis was also restricted to periods where the H_2O mixing ratio was increasing, so analysis was generally performed on 2-5 minutes of data. In addition, only chamber measurements where the correlation between $\delta_{chamber}$ and $1/q_{chamber}$ was significant ($p<0.001$) were included in this

257   analysis. A few chamber measurements where obvious non-linearity or very small changes in

258     $q_{chamber}$ occurred were also subjectively removed. Of a total of 105 chamber measurements made

259   from the 4 vegetation plots during the campaign, 99 measurements of the δ^2H_{ET}, and 97

260   measurements of $\delta^{18}O_{ET}$ and d_{ET} were retained. For the bare soil plots, 84 of the 86 chamber

261   measurements were retained for the δ^2H_{ET}, and 77 of the $\delta^{18}O_{ET}$ and d_{ET}. The eight plots were

262   sampled 2 to 4 times each day on all days except the first two days of the campaign, and the 2nd

263   and 5th of May. Sampling was restricted to between 9:00 and 17:00 LST (local solar time) as the

264   large temperature dependence of the LGR at low ambient temperatures limited the accuracy of the

265   chamber measurements.

266   Results from vegetated plots were used to determine ET flux isotopic compositions and determine

267   how ET influences d_v. The bare soil plots were used to determine the isotopic composition of soil

268   evaporation fluxes and to provide an estimate of the isotopic composition of water at the

269   evaporation front. The isotopic composition of the water at the evaporation front (δ_L) was

270   determined by rearranging the Craig and Gordon model:

271     $\delta_L = \frac{\delta_E(1-RH)+RH\,\delta_A+\varepsilon+\varepsilon_k}{\alpha}$ **(3)**

272   where the isotopic composition of the evaporation flux (δ_E) is taken from the bare soil

273   chamber measurements, relative humidity (RH) normalised to the surface temperature determined

274   from infrared surface temperature measurements (section 2.3), and the ambient vapour isotope

275   composition (δ_A) determined from Picarro *in-situ* measurements. Equilibrium fractionation and

276   enrichment factors (α, $\varepsilon=(\alpha-1)‰$) were calculated from the surface temperature measurements

277   using the equations of Horita and Wesolowski (1994), while the kinetic enrichment factor (ε_k) was

278   determined as in Gat (1996), but using the parameterisation of the exponent of the diffusion

279   coefficients described by Mathieu and Bariac (1996) and the diffusion coefficients determined by

280   Merlivat (1978).

281   **2.2.4   Iso-Forcing of ET**

282   The isotopic composition of the near-surface atmospheric water vapour is modified by surface ET

283   fluxes. The impact of ET fluxes on surface vapour isotopes varies over diurnal timescales with the

284   strength of vertical mixing in the ABL or over synoptic timescales as background moisture

285   conditions change. The magnitude and isotopic composition of the ET flux as well as the amount

286   of water vapour in the atmosphere also have an influence. The ET iso-forcing (I_{ET}) represents a

287   useful quantity to study the influence of ET fluxes on the surface vapour and is defined as:

288    $I_{ET} = \frac{F_{ET}}{H_2O}(\delta_{ET} - \delta_A)$ (8)

289   where F_{ET} is the ET flux in mol.m^{-2}.s^{-1}, H_2O is the ambient mixing ratio in mol-air.mol-

290   H_2O^{-1} measured by the local meteorological tower, and δ_{ET} and δ_A are the isotopic compositions

291   of the evaporation flux and ambient water vapour, respectively (Lee et al. 2009).

292   For each chamber measurement, a surface iso-forcing was calculated for δ^2H, $\delta^{18}O$ and D-excess

293   from the determined ET isotopic composition, as well as the hourly averaged ET flux, mixing ratio

294   and δ_A values. The importance of surface fluxes modifying surface vapour isotope composition

295   was investigated for diurnal and synoptic timescales.

2.2.5 Plant and soil sampling

296

297 Grass samples were collected three times a day for the duration of the campaign. They were

298 sampled randomly within 100 m of the instrumentation. Each sample consisted of approximately

299 10 grass leaves, which were placed in 12 ml Exetainer vials (Labco, Ceredigion, UK). The grass

300 samples were assumed to represent bulk leaf water. Soil samples were collected every 2 days

301 throughout the campaign by sampling from the top 5 cm of the soil column. They were collected

302 in 50 ml glass bottles. Soil and plant samples were stored in a fridge (4ºC), before using the

303 distillation method of West *et al*. [2006] to extract liquid water samples that were analysed on a

304 Delta V Advantage Isotope Ratio Mass Spectrometer (Thermo Fisher Scientific Corporation,

305 Massachusetts, United States). For δ^2H analysis, water samples were introduced into a H-Device

306 containing a chromium reactor, while for the $\delta^{18}O$ analysis, water samples were equilibrated with

307 CO_2 on a Gas Bench II chromatography column (Thermo Fisher Scientific Corporation,

308 Massachusetts, USA) before being transferred to the IRMS for analysis.

2.3 ET Fluxes and Meteorological measurements

309

310 To measure ET fluxes, an eddy covariance system comprising a Campbell Scientific 3D sonic

311 anemometer (CSAT-3, Campbell Scientific, Logan, UT, USA) along with a LiCOR 7500 (Li-

312 7500, LiCor Biosciences, Lincoln, NB, USA) analyser was installed at an elevation of 2.5 m. The

313 system was located approximately 10 m from the stable isotope observation tower and sampled at

314 10 Hz, with flux averages output at 30 minute intervals. The ET fluxes from the eddy covariance

315 tower are used to quantify the Iso-Forcing of ET on the overlying atmosphere.

316 A meteorological tower was co-located with the eddy covariance system, providing

317 complementary data to aid in the interpretation of measurements. The tower comprised a Kipp and

318   Zonen CNR4 radiometer, Apogee infrared surface temperature, RIMCO rainguage, Vaisala

319   HMP75C temperature and humidity probe, RM Young wind sentry (wind speed and direction),

320   Huskeflux ground heat flux plate and Vaisala BaroCap barometric pressure sensor. Both

321   meteorological tower data and eddy-covariance data were inspected visually to detect and remove

322   spikes. The low-frequency eddy covariance data (30 minute resolution) were corrected for

323   coordinate rotation (Finnigan et al. 2003) and density effects (Leuning, 2007) using the PyQC

324   software tool (available from code.google.com/p/eddy).

325   **2.4   Radon-222 measurements**

326   The naturally occurring radioactive gas radon (^{222}Rn) is predominantly of terrestrial origin and its

327   only atmospheric sink is radioactive decay (Zahorowski et al. 2004). The surface flux density of

328   radon is relatively constant in space and time, and since the half-life is much greater than ABL

329   mixing timescales, it is an ideal tracer of vertical mixing strength within the ABL (Chambers et al.

330   2014; Griffiths et al. 2013; Williams et al. 2010). Hourly radon concentrations were measured by

331   an Alpha Guard (Saphymo GmbH, Frankfurt, Germany) placed in a ~20 L enclosure. The

332   enclosure was purged at ~15 l.min^{-1} with a vacuum pump (2107 Series, Thomas, Wisconsin, USA)

333   that sampled from a height of 2 m through 10 mm O.D. PTFE tubing. Radon measurements were

334   used to aid the interpretation of the diurnal variations in vertical mixing (see Griffiths et al. 2013).

335   **3   Results**

336   **3.1   Meteorological observations**

337   The two-week campaign was conducted under predominantly calm meteorological conditions. The

338   last rain event was 10 days prior to the campaign, after which clear skies saw the soil dry to a

339   moisture content close to minimum values observed for the site (Figure 4). In the middle of the

340   campaign (May 2nd), a cold front moved across south eastern Australia, producing cloudy

341   conditions and 1.4 mm of precipitation at the site. No change in soil moisture was observed over

342   the 0-10 cm soil layer following the rain event.

343   Wind directions were variable during the campaign (see figure S2a and b). Figure S3 shows that

344   from 27th to 30th April, dominant daytime wind directions were mainly from the east. After May

345   3rd winds were from the south, except on the 7th and 8th when the wind was from the west and

346   had a fetch from the adjacent forest. At other times the fetch did not overlap the forested site. Daily

347   maximum temperatures on clear days ranged from 16 to 23ºC, whilst night time minimum

348   temperatures fell to between 8 and -4°C. From May 7th onwards nocturnal temperatures fell below

349   zero. On clear nights the surface temperature fell below dew point temperature, indicating dew

350   fall. Apart from the night of the 27-28th April and the cloudy nights between 1st and 3rd May, the

351   surface temperature fell below dew point temperature and dew or frost was observed in the

352   morning, although heavier from the 7th May onwards.

353   Radon concentrations were low during the day, when the convective boundary layer reached its

354   maximum height, and high at night, when radon emissions were confined within the shallow

355   nocturnal boundary layer. The accumulation at night was variable indicating a varying degree of

356   nocturnal stability, mixing depth and occurrence of transient mixing events (Griffiths et al. 2013).

357   There was general agreement between high nocturnal radon concentrations and low wind speeds,

358   but no direct relationship. The lack of a direct relationship indicates that radon can provide

359   additional information about nocturnal mixing and surface exchange that compliments standard

360   meteorological measurements (Chambers et al. 2015a, 2015b; Williams et al. 2013).

361   ET fluxes were in general quite low, reflecting the low soil moisture content. The ET flux did show

362   a marked increase the day after the small rain event on May 2nd and noticeably smaller fluxes

363   were observed after the first night frost was observed. The health of the grass visibly deteriorated

364   from the 7th May, coinciding with frost formation.

365   **3.2   Relationship between δ^2H and $\delta^{18}O$ of the different water pools**

366   A summary of the isotopic composition of all observed and modelled water pools are presented

367   in Figure 6. The local MWL (Hughes and Crawford, 2013) is to the left of the global MWL (Craig,

368   1961), illustrating the characteristically high D-excess of precipitation in the region (Crawford et

369   al., 2013). Ambient vapour observations aligned closely with the local MWL, but with a

370   distribution that fell both to the left and right of the local MWL. Alignment between observations

371   and the MWL show that equilibrium fractionation was the dominant process modifying δ^2H and

372      $\delta^{18}O$ in water vapour, while non-equilibrium kinetic processes shift observations away from the

373   MWL and are more easily observed for d_v measurements.

374   Plant and soil water pools were enriched relative to the vapour and distributed to the right of the

375   MWL, indicating evaporative enrichment. Soil water isotopes at the evaporation front (δ_L) were

376   very enriched and had lower D-excess values (50±12, 31±3.8 and -131±22 ‰ for δ^2H, $\delta^{18}O$ and

377   D-excess) relative to the average soil moisture between 0 and 5 cm (-15±4.2, 2.6±2.5 and -36±17

378   ‰ for δ^2H, $\delta^{18}O$ and D-excess). Low D-excess and enriched isotopes indicated large evaporative

379   enrichment under non-equilibrium conditions consistent with $\delta^{18}O$ soil profile measurements of

380   Dubbert *et al*., (2013) and δ^2H profiles of Allison *et al*., (1983). The uncertainty of modelled

381   isotope values was most sensitive to parameterisation of the Craig-Gordon model. Changing the

382   diffusion coefficient exponent (*n*) had the greatest impact on modelled soil water (*n*=0.66, 42.7±12,

383 21.8±3.8 and -130.8±22 ‰). However, changing parameterisation did not change the conclusion

384 that soil moisture at the evaporation front was heavily enriched with very low D-excess values.

385 ET flux isotopic compositions from vegetated chambers were enriched relative to vapour and

386 distributed to the right of the MWL (slope = 3.2). Similar isotopic compositions were measured

387 from bare soil and vegetated chambers. Mean and standard deviations (1σ) for vegetated and soil

388 chambers were -47.1 (±13) and -50.2 (±11) for δ^2H, -5.03 (±3.8) and -6.3 (±2.7)‰ for δ^{18}, and -

389 6.3 (±23) and -0.12 (±15)‰ for D-excess, respectively. The similar ET isotopic composition from

390 bare soil and vegetated chambers could indicate soil evaporation was the dominant process

391 contributing to total ET. However, as pointed out in the discussion (section 4.3), convergence of

392 soil evaporation and transpiration isotope compositions as the soil evaporation source becomes

393 progressively enriched (and D-excess lower), probably makes it difficult to identify the dominant

394 process from these observations. Nevertheless, since the last significant rain event prior to the

395 campaign, progressive reduction of D-excess of moisture at the evaporation front and to a lesser

396 extent in the 0-5 cm layer caused low D-excess of overall ET fluxes compared to d_v. This would

397 indicate that ET imposes a negative forcing on d_v.

398 Temporally, a clear trend was not observed for ET isotopic compositions over the measured

399 portion of the diurnal cycle or over the campaign. No measurements were made at night or during

400 the rapidly changing conditions of the morning transition, which may have led to our data missing

401 some observed changes in ET isotope compositions.

402 **3.3   *In-situ* water vapour isotopes and ET iso-forcing**

403 Observed water vapour mixing ratios and stable isotope compositions are shown in Figure 7. δ^2H

404 and $\delta^{18}O$ variability was similar, reflecting changes in both the synoptic and local meteorology.

405   Prior to the rain event (May 2nd), relatively moist conditions (higher H_2O mixing ratios) were

406   observed as air was transported from the warmer ocean off the east coast of Australia (see wind

407   direction in figure S3). After May 5th, transport of air masses from the colder sea surface south of

408   continental Australia brought drier conditions to the site (lower H_2O mixing ratios). Moisture

409   source regions were confirmed by backward air trajectories calculated using the Stochastic Time-

410   Inverted Lagrangian Transport Model (STILT; Lin *et al.* (2003) not shown). These two time

411   periods are hereinafter referred as "wet period" (before May 2nd) and "dry periods" (after May

412   5th). The wet period coincided with more enriched isotopes and less diurnal variability. In the later

413   part of the campaign, a reproducible diurnal cycle for δ^2H and $\delta^{18}O$ was observed (see Figure 8

414   for diurnal composites), presenting a sharp increase at sunrise before decreasing from mid-morning

415   (when vertical mixing increased) until the next sunrise. These observations emphasise the complex

416   relationship between stable isotope observations in water vapour and both local and synoptic scale

417   meteorology.

418   The d_v dataset showed a robust diurnal cycle of high values in the day and low values at night,

419   consistent with what has been observed across a growing number of locations (Bastrikov et al.

420   2014; Berkelhammer et al. 2013; Simonin et al. 2014; Welp et al. 2012; Zhao et al. 2014). Wet

421   period daytime d_v values were on average lower than those observed for the dry period. Nocturnal

422   d_v was consistently lower during the night, but variable from night to night and across individual

423   nights, with no clear difference observed between wet and dry periods. Contrasting daytime

424   measurements of wet and dry periods indicate a role of large scale processes, whilst the lack of

425   contrast for nocturnal observation show the importance of local processes.

426   The I_{ET} was always positive for δ^2H and $\delta^{18}O$ and mostly negative for D-excess, but showed large

427   variability across individual days (Figure 7). I_{ET} was most sensitive to the magnitude of the ET

428   fluxes, producing the greatest forcing on ambient vapour in the middle of the day. The I_{ET} time

429   series did not correspond to temporal variability of vapour δ^2H, $\delta^{18}O$ or D-excess. δ^2H and $\delta^{18}O$

430   often decreased during the day while I_{ET} was positive. Whilst the high d_v values observed during

431   the day were associated with negative isoforcing, over the course of the campaign highest daytime

432   d_v values did not correspond to the least negative I_{ET}. These observations illustrate that local ET

433   fluxes were not overly important for day-to-day and diurnal d_v trends.

434   The level of agreement between the analysers presented some uncertainty for calculation of the D-

435   excess isoforcing. The sign of the isoforcing is dependent on the difference between d_v and d_{ET}

436   (equation 8). In some cases this difference was small and within the range of agreement between

437   the two analysers. While this caused problems for accurate calculation of the absolute values of

438   D-excess isoforcing, for all chamber measurements passing our QC requirements, D-excess

439   decreased with concentration. This indicates that for all measurements the D-excess, isoforcing

440   was negative.

441   **3.4   Relationship between water vapour isotopes and local meteorology**

442   The relationships between local meteorological variables and water vapour isotopes were

443   examined to interpret the role of local processes (Table 1). Regression statistics are shown for both

444   hourly observations and average daytime values (between 11:00 and 16:00 LST). Selecting

445   daytime measurements removes variability associated with transition between the stable nocturnal

446   and daytime convective boundary layer, as well as nocturnal periods when local surface

447   equilibrium exchange and dewfall affect vapour isotope compositions. Correlations determined

448   using only measurements in the middle of the day therefore provide a better indicator of how local

449   meteorology and ET isotopic composition modified ambient water vapour isotope ratios from day

450   to day.

451   Correlations calculated with hourly data were weak for $\delta^{18}O$ and δ^2H. Only correlations with air

452   temperature (R^2=0.24 and 0.04, respectively) and mixing ratio (R^2=0.2 for both isotopes) were

453   significant, and δ^2H also showed a weak correlation with RH (R^2=0.09). For daytime observations,

454   only δ^2H showed a significant correlation with daytime I_{ET} (R^2=0.45, p<0.05), but the slope was

455   negative in contrast to positive isoforcing. The weak relationships with local meteorology indicate

456   the importance of larger scale precipitation processes and atmospheric mixing occurring as

457   moisture was transported to the site.

458   As the diurnal cycle for d_v was consistent with growth and decay of the ABL, strong relationships

459   were observed with air temperature and RH for the hourly observations. While the local air

460   temperature and RH could modify d_{ET} on diurnal timescales and in turn local d_v, the chamber

461   measurements showed relatively constant d_{ET}. These correlations therefore result from the

462   coincident diurnal variation of the d_v, RH and air temperature.

463   Daytime average d_v showed significant correlations with the air temperature, RH, ET flux and

464   mixing ratio. The relationship with ET fluxes was weak (R^2=0.3) and positive, but as negative D-

465   excess isoforcing was observed, a negative relationship would be expected. Likewise, the slope

466   between air temperature and d_v was negative, counter to what theory would predict for local or

467   remote moisture sources. The strongest relationship was observed with daytime RH ($R^2 = 0.74$),

468   which had a negative slope (-0.52‰.%$^{-1}$) consistent with an inverse relationship between d_v and

469   RH for a large unchanging evaporation source. The strong relationship of d_v with the daytime RH

470   could indicate an important role for the evaporation conditions at remote moisture sources, as is

471   discussed below in Section 4.2.

472   **3.5   Diurnal variability of vapour isotopes**

473   Diurnal composites were divided into dry and wet periods and are shown in Figure 8. At sunrise

474   (approximately 06:30 LST) surface heating initiated vertical mixing, shown by the radon

475   concentration maximum, causing temperature and ET flux to increase and RH decrease. Weak

476   vertical mixing immediately after sunrise and injection of ET into the still shallow surface layer

477   caused near-surface humidity to increase. Similarly for δ^2H and $\delta^{18}O$, the observed spike

478   immediately after sunrise was likely caused by ET fluxes with an enriched heavy isotope

479   composition, possibly from re-evaporation of dewfall. During the dry period, vapour δ^2H and $\delta^{18}O$

480   increased more steeply, caused by the combination of a shallower surface layer observed at the

481   start of the morning transition, shown by higher radon concentrations, and more dewfall on the

482   surface providing a greater initial evaporation source. Rapidly decreasing radon concentrations

483   during this morning ABL transition caused by vigorous vertical mixing entraining air from the

484   residual layer of the previous day diluted ET fluxes and caused the δ^2H, $\delta^{18}O$ and the mixing ratio

485   to first stabilise and then decrease. ET fluxes rapidly increased as the ABL grew, but were not

486   large enough to offset the dilution by dry air being mixed down from above or stop depletion of

487   surface δ^2H and $\delta^{18}O$.

488   The d_v also increased after sunrise, but aligned more closely to when strong vertical mixing

489   commenced, as shown by the close agreement with radon concentrations. The D-excess isoforcing

490   was negative, evidence that d_v increased from encroachment mixing as the new mixed layer grew

491   in depth and not ET fluxes. The dry period showed a greater increase in d_v during the morning

492   transition, likely the result of higher d_v in background water vapour and greater differences

493   between the d_v of the residual and nocturnal layer.

494   In the afternoon, d_v decreased back to values similar to those observed prior to sunrise, with a

495   simultaneous decrease in solar insolation, ET and a decay of convective mixing. Radon shows how

496   reduction in vertical mixing causes the concentration of tracers emitted from the surface to

497   increase. So while ET decreased, small fluxes were still observed well after 18:00, when large

498   changes in $\delta^{18}O$ and d_v were observed. Hence, as the I_{ET} was positive and negative for $\delta^{18}O$ and

499   D-excess, respectively, small ET fluxes into a poorly mixed surface layer may have led to observed

500   changes.

501   During the night, dew fall caused δ^2H and $\delta^{18}O$ to decrease as heavy isotopes were removed in

502   condensation, especially during the dry period when greater surface cooling was observed.

503   However, dew formation is an equilibrium processes so did not affect d_v. Composites of dry and

504   wet period nocturnal d_v measurements do not show clear nocturnal trends, but individual nights

505   showed considerable variability. A regression of nocturnal d_v with radon concentrations produced

506   a significant negative relationship (p<0.001, $R^2 = 0.31$), indicating that atmospheric stability has

507   some control over nocturnal d_v. High radon is associated with the most stable atmospheres,

508   enhancing the effect of surface exchange in the early evening. Low radon on the other hand, is

509   associated with periods of atmospheric turbulence in which moisture above the nocturnal inversion

510   with a high d_v is mixed down towards the surface.

511

4   Discussion

As has been previously observed (Steen-Larsen et al. 2013; Welp et al. 2012) and predicted by isotopic models (Gat, 1996), our observations showed water vapour $\delta^2 H$ and $\delta^{18}O$ are controlled by different atmospheric and hydrological processes than d_v. The diurnal cycle was the dominant mode of variability for d_v, consistent with previous studies for a range of ecosystems (Simonin et al. 2014; Welp et al. 2012; Zhao et al. 2014). However, results also showed that D-excess variability was controlled by local meteorological conditions and surface exchange at night, ABL growth and decay during transitional periods between the nocturnal and convective ABL, and larger scale processes in the middle of the day.

4.1   Entrainment and the d_v diurnal cycle

The radon measurements showed that when the depth of the ABL was rapidly changing through the morning and evening transitions, entrainment from the residual layer and ET fluxes into a rapidly decaying convective boundary layer caused the observed d_v diurnal cycle. Between these transitions, when mixing extends to the capping inversion, entrainment fluxes introduce an additional moisture source from the free troposphere that could modify surface vapour isotopic compositions. Air above the ABL is drier and moisture is more depleted than at the surface. Drying and depleting trends for water vapour, $\delta^2 H$ and $\delta^{18}O$ throughout the day, particularly during the dry period (Figure 8), indicate an important role for entrainment from the free troposphere. Whether this moisture flux impacts on d_v is less clear, as it remained reasonably stable once a maximum was reached after the morning transition period. The sign of the isoforcing of moisture entrained from the free troposphere is uncertain, as few free tropospheric d_v measurements exist (He and Smith, 1999; Samuels-Crow et al., 2014). Nevertheless, d_v values did not show a clear

534   trend until vertical mixing began decaying later in the afternoon, so free tropospheric d_v probably

535   has a similar value to moisture already residing in the ABL.

536   **4.2   Remote hydrometeorological processes**

537   While the main focus of this study was to examine the role of local land-atmosphere exchange for

538   the diurnal variability of d_v, the synoptic context of measurements warrants further examination

539   for comparison against previous studies of d_v diurnal cycles. The slope between daytime RH and

540   d_v (-0.52‰.%$^{-1}$, Table 1) was similar to those determined for measurements over the

541   Mediterranean sea and different ocean basins (between -0.43 and -0.53 ‰.%$^{-1}$) (Kurita, 2011;

542   Pfahl and Wernli, 2008; Steen-Larsen et al. 2014, 2015; Uemura et al. 2008). Aemisegger *et al.*

543   (2014) showed that this robust relationship is not restricted to coastal locations or measurements

544   over the ocean surface. Using a trajectory model to investigate continental moisture recycling in

545   Europe, they found a similar relationship between d_v and RH of remote moisture sources during

546   the cold season (-0.57 ‰.%$^{-1}$), but not for warm season observations. They concluded moisture

547   recycling is weakest during winter, causing d_v to retain the signature of the RH of oceanic moisture

548   sources, while in summer moisture recycling increased and attenuated the relationship. Similarities

549   with their winter data indicates that our daytime d_v measurements were at least partly determined

550   by RH at the oceanic moisture source.

551   Along an air masses back trajectory, entrainment fluxes from the free troposphere could be a major

552   driver of daytime d_v variability. Mixing of warm dry air down to the surface, presumably with a

553   relatively high D-excess (He and Smith, 1999; Samuels-Crow et al., 2014), would give the same

554   negative relationship between d_v and RH observed here. However, for a strong relationship

555   between d_v and RH, there must be a dominant moisture source. For the fraction of entrained air in

556 the ABL to cause the strong linear relationship, the D-excess of vapour and RH in both the ABL

557 and free troposphere must be reasonably constant, as in a two source mixing model. Considering

558 the variability of synoptic scale weather patterns observed (section 3.1), this seems unlikely. Thus,

559 while we cannot definitively rule out the importance of entrainment along back trajectories, it

560 seems more likely that the d_v vs RH relationship was derived from a large unchanging moisture

561 source such as the ocean.

562 A practical application of the d_v/RH relationship introduced by Aemisegger *et al.* (2014) was to

563 determine the D-excess of the liquid moisture source. Based on the closure assumption of Merlivat

564 and Jouzel (1979), it was shown when RH is 100%, d_v is equal to the D-excess of the liquid

565 moisture source. If no further kinetic fractionation or mixing of vapour with a different d_v/RH

566 occurred between the point of evaporation and measurement location, extrapolating the regression

567 between d_v and RH to 100% RH gives an estimate of moisture source D-excess. For our

568 measurements, a value of -8‰ was determined, remarkably similar to the D-excess determined for

569 ocean water off the east coast of Australia by Xu *et al.* (2012) using a global ocean model. In

570 contrast to recent literature (Simonin et al. 2014; Welp et al. 2012; Zhao et al. 2014), this suggests

571 that although the common diurnal cycle was observed, daytime observations are potentially a

572 tracer of RH at the oceanic moisture source, but it is likely restricted to periods when moisture

573 recycling is weak.

574 Whilst we have shown a relationship between the RH and d_v consistent with an oceanic vapour

575 source, the consistency of the relationship over longer time periods is uncertain. Indeed, it may be

576 the reason why we show a strong relationship whereas the study of Welp *et al.* (2012) did not for

577 six mid-latitude sites in China and the USA, where longer datasets were available. As pointed out

578 earlier, lowers slopes and weaker relationships result from stronger moisture recycling, which

579 indicates moisture recycling and soil moisture state may be the most important variable controlling

580 the relationship between d_v and RH. Here we present data from after an extended dry period, where

581 the dominant moisture source is the ocean surrounding the Australian continent. So during wetter

582 periods, increase in the local and remote moisture recycling probably weaken the relationship

583 between local d_v and RH (Aemisegger et al. 2014). However, for locations such as semi-arid

584 Australia where extended dry periods prevail, the relationship between d_v and RH may be

585 reasonably robust and prevail as a tracer of oceanic evaporative environments.

586 4.3 Controls of d_{ET}

587 The chamber d_{ET} measurements showed ET fluxes imposed a negative isoforcing on d_v, in contrast

588 to interpretations in previous studies investigating d_v variability on diurnal time scales (Simonin et

589 al. 2014; Zhao et al. 2014). However, it is expected that the sign and magnitude of the D-excess

590 isoforcing would vary both spatially and temporally, in particular with soil moisture state. After a

591 rain event, soil moisture D-excess would decrease following a pseudo-Rayleigh process (Barnes

592 and Allison, 1988). Therefore, immediately after a rainfall event, d_{ET} would be higher and probably

593 impose a positive isoforcing. Here the negative d_{ET} caused the d_v to decrease rapidly as convective

594 mixing shut down. When isoforcing is positive after a rain event, the diurnal cycle observed here

595 and elsewhere may therefore not be observed. Although equilibration between liquid and vapour

596 pools, as eluded to by Simonin *et al.*, (2014), may still help maintain observed trends. As soil dries,

597 a tipping point when the ET fluxes switch from positive to negative isoforcing will be observed.

598 This has implications for studies attempting to use d_v as a tracer of continental moisture recycling,

599 as the large spatial variability of rainfall and the associated soil moisture state would lead to large

600   spatial and temporal variability for d_{ET}. Although, the strongest moisture recycling is expected for

601   wet soils when d_{ET} is higher, variability in d_{ET} may still be important.

602   Relative magnitudes of evaporation and transpiration fluxes are important for d_{ET}, as the two

603   processes could have different D-excess values and could vary strongly between precipitation or

604   irrigation events. The classical view of ET isotope fluxes is that transpiration has an isotopic

605   composition closer to the source moisture than evaporation, so a higher D-excess. However,

606   greater fractionation of the evaporation source pool causes its D-excess value to decrease over

607   time, so the D-excess of the fluxes would converge overtime. The impact of converging isotopic

608   signatures of ET component fluxes on moisture recycling would depend on the land surface type,

609   but would constitute an important variable influencing the D-excess of local and remote moisture

610   recycling. Further studies investigating how ET partitioning and drying of soil moisture reservoirs

611   following irrigation or precipitation events would lead to a better understanding of how moisture

612   recycling influences the ambient d_v on continental and local scales.

613   **5   Conclusions**

614   To determine how local ET fluxes modified water vapour D-excess, in-situ observations were

615   collected in a semi-arid region of south-eastern Australia. The diurnal cycle exhibited high values

616   during the day and low values at night, reflected findings from previous studies. With chamber

617   based measurements of isotopic compositions in evaporative fluxes, it was shown that local ET

618   fluxes exhibited a negative forcing on the ambient water vapour D-excess that could not explain

619   the high daytime values. A strong negative relationship was observed between the locally

620   measured relative humidity and vapour D-excess during the daytime, consistent with relationships

621 observed for oceanic moisture sources. During the evening transition, collapse of the convective

622 boundary layer and small ET fluxes with negative D-excess isoforcing were responsible for

623 lowering the D-excess of water vapour near the surface. In addition, a negative nocturnal

624 correlation between D-excess in water vapour and radon concentrations indicated transient

625 nocturnal mixing events shifted the D-excess back towards the higher values observed during the

626 day, with the most stable (least turbulent) nights producing the lowest D-excess values. In the

627 morning, encroachment and entrainment of high D-excess air from above caused D-excess of

628 surface vapour to increase back to the synoptic values.

629 Overall, it was found that the magnitude of the D-excess diurnal cycle was controlled

630 predominantly by interplay between synoptic forcing and local ABL processes and was modified

631 further by nocturnal surface exchange processes and turbulent mixing. The low D-excess of the

632 ET fluxes determined from flux chambers in this study illustrated that the impact of large scale

633 moisture recycling may be both spatially and temporally variable, depending on the soil moisture

634 state. This has implications for studies using D-excess to investigate moisture recycling.

643 Tremain for access to the Baldry Hydrological Observatory and surrounding farmland, Chris

644 Dimovski for performing plant and soil water extractions, and Barbara Neklapilova analysis of

645 plant and soil water samples.

646 For access to the data used in this paper contact Dr Stephen Parkes by email

647 (stephen.parkes@kaust.edu.sa).

648

649

650 **7   References**

651 Aemisegger, F., Pfahl, S., Sodemann, H., Lehner, I., Seneviratne, S. I. and Wernli, H.: Deuterium
652 excess as a proxy for continental moisture recycling and plant transpiration, Atmos. Chem. Phys.,
653 14(8), 4029–4054, doi:10.5194/acp-14-4029-2014, 2014.

654 Allison, G. B., Barnes, C. J. and Hughes, M. W.: The distribution of deuterium and 18O in dry
655 soils 2. Experimental, J. Hydrol., 64(1-4), 377–397, doi:10.1016/0022-1694(83)90078-1, 1983.

656 Barnes, C. J. and Allison, G. B.: Tracing of water movement in the unsaturated zone using stable
657 isotopes of hydrogen and oxygen, J. Hydrol., 100(1-3), 143–176, doi:10.1016/0022-
658 1694(88)90184-9, 1988.

659 Bastrikov, V., Steen-Larsen, H. C., Masson-Delmotte, V., Gribanov, K., Cattani, O., Jouzel, J. and
660 Zakharov, V.: Continuous measurements of atmospheric water vapour isotopes in western Siberia
661 (Kourovka), Atmos. Meas. Tech., 7(6), 1763–1776, doi:10.5194/amt-7-1763-2014, 2014.

662 Berkelhammer, M., Hu, J., Bailey, A., Noone, D. C., Still, C. J., Barnard, H., Gochis, D., Hsiao,
663 G. S., Rahn, T. and Turnipseed, A.: The nocturnal water cycle in an open-canopy forest, J.
664 Geophys. Res. Atmos., 118(17), 10,210–225,242, doi:10.1002/jgrd.50701, 2013.

665 Chambers, S. D., Wang, F., Williams, A. G., Xiaodong, D., Zhang, H., Lonati, G., Crawford, J.,
666 Griffiths, A. D., Ianniello, A. and Allegrini, I.: Quantifying the influences of atmospheric stability
667 on air pollution in Lanzhou, China, using a radon-based stability monitor, Atmos. Environ., 107,
668 233–243, doi:10.1016/j.atmosenv.2015.02.016, 2015a.

669 Chambers, S. D., Williams, A. G., Crawford, J. and Griffiths, A. D.: On the use of radon for
670 quantifying the effects of atmospheric stability on urban emissions, Atmos. Chem. Phys. Discuss.,
671 14(18), 25411–25452, doi:10.5194/acpd-14-25411-2014, 2014.

672 Chambers, S. D., Williams, A. G., Crawford, J. and Griffiths, A. D.: On the use of radon for

673 quantifying the effects of atmospheric stability on urban emissions, Atmos. Chem. Phys., 15(3),
674 1175–1190, doi:10.5194/acp-15-1175-2015, 2015b.

675 Craig, H.: Isotopic Variations in Meteoric Waters, Sci. , 133 (3465), 1702–1703,
676 doi:10.1126/science.133.3465.1702, 1961.

677 Craig, H. and Gordon, L. I.: Deuterium and oxygen-18 variations in the ocean and marine
678 atmosphere, in Stable isotopes in oceanographic studies and paleotemperatures, Proceedings,
679 Spoleto, Italy., edited by E. Tongiogi, pp. 9–130, Pisa, Italy., 1965.

680 Crawford, J., Hughes, C. E. and Parkes, S. D.: Is the isotopic composition of event based
681 precipitation driven by moisture source or synoptic scale weather in the Sydney Basin, Australia?,
682 J. Hydrol., 507(0), 213–226, doi:http://dx.doi.org/10.1016/j.jhydrol.2013.10.031, 2013.

683 Dansgaard, W.: Stable isotopes in precipitation, Tellus, 16(4), 436–468, doi:10.1111/j.2153-
684 3490.1964.tb00181.x, 1964.

685 Decker, M., Pitman, A. and Evans, J.: Diagnosing the seasonal land–atmosphere correspondence
686 over northern Australia: dependence on soil moisture state and correspondence strength definition,
687 Hydrol. Earth Syst. Sci., 19(8), 3433–3447, doi:10.5194/hess-19-3433-2015, 2015.

688 Dubbert, M., Cuntz, M., Piayda, A., Maguás, C. and Werner, C.: Partitioning evapotranspiration
689 – Testing the Craig and Gordon model with field measurements of oxygen isotope ratios of
690 evaporative fluxes, J. Hydrol., 496, 142–153, doi:10.1016/j.jhydrol.2013.05.033, 2013.

691 Evans, J. P. and McCabe, M. F.: Regional climate simulation over Australia's Murray-Darling
692 basin: A multitemporal assessment, J. Geophys. Res. Atmos., 115(D14), n/a–n/a,
693 doi:10.1029/2010JD013816, 2010.

694 Finnigan, J. J., Clement, R., Malhi, Y., Leuning, R. and Cleugh, H. A.: A Re-Evaluation of Long-
695 Term Flux Measurement Techniques Part I: Averaging and Coordinate Rotation, Boundary-Layer
696 Meteorol., 107(1), 1–48, doi:10.1023/A:1021554900225, 2003.

697 Froehlich, K., Kralik, M., Papesch, W., Rank, D., Scheifinger, H. and Stichler, W.: Deuterium
698 excess in precipitation of Alpine regions – moisture recycling, Isotopes Environ. Health Stud.,
699 44(1), 61–70, doi:10.1080/10256010801887208, 2008.

700 Gat, J. R.: OXYGEN AND HYDROGEN ISOTOPES IN THE HYDROLOGIC CYCLE, Annu.
701 Rev. Earth Planet. Sci., 24(1), 225–262, doi:10.1146/annurev.earth.24.1.225, 1996.

702 Gat, J. R., Bowser, C. J. and Kendall, C.: The contribution of evaporation from the Great Lakes to
703 the continental atmosphere: estimate based on stable isotope data, Geophys. Res. Lett., 21(7), 557–
704 560, doi:10.1029/94GL00069, 1994.

705 Gat, J. R., Klein, B., Kushnir, Y., Roether, W., Wernli, H., Yam, R. and Shemesh, A.: Isotope
706 composition of air moisture over the Mediterranean Sea: an index of the air–sea interaction pattern,
707 Tellus B, 55(5), 953–965, doi:10.1034/j.1600-0889.2003.00081.x, 2003.

708 Griffiths, A. D., Parkes, S. D., Chambers, S. D., McCabe, M. F. and Williams, A. G.: Improved
709 mixing height monitoring through a combination of lidar and radon measurements, Atmos. Meas.
710 Tech., 6(2), 207–218, doi:10.5194/amt-6-207-2013, 2013.

711 Harding, K. J. and Snyder, P. K.: Modeling the Atmospheric Response to Irrigation in the Great
712 Plains. Part I: General Impacts on Precipitation and the Energy Budget, J. Hydrometeorol., 13(6),

713   1667–1686, doi:10.1175/JHM-D-11-098.1, 2012.

714   He, H. and Smith, R. B.: Stable isotope composition of water vapor in the atmospheric boundary
715   layer above the forests of New England, J. Geophys. Res. Atmos., 104(D9), 11657–11673,
716   doi:10.1029/1999JD900080, 1999.

717   Horita, J. and Wesolowski, D. J.: Liquid-vapor fractionation of oxygen and hydrogen isotopes of
718   water from the freezing to the critical temperature, Geochim. Cosmochim. Acta, 58(16), 3425–
719   3437, doi:http://dx.doi.org/10.1016/0016-7037(94)90096-5, 1994.

720   Huang, L. and Wen, X.: Temporal variations of atmospheric water vapor δD and $\delta 18O$ above an
721   arid artificial oasis cropland in the Heihe River Basin, J. Geophys. Res. Atmos., 119(19),
722   2014JD021891, doi:10.1002/2014JD021891, 2014.

723   Hughes, C. E. and Crawford, J.: Spatial and temporal variation in precipitation isotopes in the
724   Sydney Basin, Australia, J. Hydrol., 489(0), 42–55,
725   doi:http://dx.doi.org/10.1016/j.jhydrol.2013.02.036, 2013.

726   Jana, R. B., Ershadi, A. and McCabe, M. F.: Examining the relationship between intermediate-
727   scale soil moisture and terrestrial evaporation within a semi-arid grassland, Hydrol. Earth Syst.
728   Sci., 20(10), 3987–4004, doi:10.5194/hess-20-3987-2016, 2016.

729   Keeling, C. D.: The concentration and isotopic abundances of atmospheric carbon dioxide in rural
730   areas, Geochim. Cosmochim. Acta, 13(4), 322–334, doi:10.1016/0016-7037(58)90033-4, 1958.

731   Kurita, N.: Origin of Arctic water vapor during the ice-growth season, Geophys. Res. Lett., 38(2),
732   n/a–n/a, doi:10.1029/2010GL046064, 2011.

733   Lai, C.-T. and Ehleringer, J.: Deuterium excess reveals diurnal sources of water vapor in forest air,
734   Oecologia, 165(1), 213–223, doi:10.1007/s00442-010-1721-2, 2011.

735   Lee, X., Griffis, T. J., Baker, J. M., Billmark, K. A., Kim, K. and Welp, L. R.: Canopy-scale kinetic
736   fractionation of atmospheric carbon dioxide and water vapor isotopes, Global Biogeochem.
737   Cycles, 23(1), GB1002, doi:10.1029/2008GB003331, 2009.

738   Leuning, R.: The correct form of the Webb, Pearman and Leuning equation for eddy fluxes of
739   trace gases in steady and non-steady state, horizontally homogeneous flows, Boundary-Layer
740   Meteorol., 123(2), 263–267, doi:10.1007/s10546-006-9138-5, 2007.

741   Lin, J. C., Gerbig, C., Wofsy, S. C., Andrews, A. E., Daube, B. C., Davis, K. J. and Grainger, C.
742   A.: A near-field tool for simulating the upstream influence of atmospheric observations: The
743   Stochastic Time-Inverted Lagrangian Transport (STILT) model, J. Geophys. Res., 108, 4493,
744   doi:10.1029/2002JD003161, 2003.

745   Lu, X., Liang, L. L., Wang, L., Jenerette, G. D., McCabe, M. F. and Grantz, D. A.: Partitioning of
746   evapotranspiration using a stable isotope technique in an arid and high temperature agricultural
747   production system, Agric. Water Manag., In Press, ,
748   doi:http://dx.doi.org/10.1016/j.agwat.2016.08.012, 2016.

749   Masson-Delmotte, V., Jouzel, J., Landais, A., Stievenard, M., Johnsen, S. J., White, J. W. C.,
750   Werner, M., Sveinbjornsdottir, A. and Fuhrer, K.: GRIP Deuterium Excess Reveals Rapid and
751   Orbital-Scale Changes in Greenland Moisture Origin, Sci. , 309 (5731), 118–121,
752   doi:10.1126/science.1108575, 2005.

753   Mathieu, R. and Bariac, T.: A numerical model for the simulation of stable isotope profiles in
754   drying soils, J. Geophys. Res. Atmos., 101(D7), 12685–12696, doi:10.1029/96JD00223, 1996.

755   McCabe, M. F., Ershadi, A., Jimenez, C., Miralles, D. G., Michel, D. and Wood, E. F.: The
756   GEWEX LandFlux project: evaluation of model evaporation using tower-based and globally
757   gridded forcing data, Geosci. Model Dev., 9(1), 283–305, doi:10.5194/gmd-9-283-2016, 2016.

758   McCabe, M. F., Franks, S. W. and Kalma, J. D.: Calibration of a land surface model using multiple
759   data sets, J. Hydrol., 302(1–4), 209–222, doi:http://dx.doi.org/10.1016/j.jhydrol.2004.07.002,
760   2005.

761   Merlivat, L.: Molecular diffusivities of H2O16O, HD16O, and H218O in gases, J. Chem. Phys.,
762   69(6), 2864, doi:10.1063/1.436884, 1978.

763   Merlivat, L. and Jouzel, J.: Global climatic interpretation of the deuterium-oxygen 18 relationship
764   for precipitation, J. Geophys. Res. Ocean., 84(C8), 5029–5033, doi:10.1029/JC084iC08p05029,
765   1979.

766   Noone, D., Risi, C., Bailey, A., Berkelhammer, M., Brown, D. P., Buenning, N., Gregory, S.,
767   Nusbaumer, J., Schneider, D., Sykes, J., Vanderwende, B., Wong, J., Meillier, Y. and Wolfe, D.:
768   Determining water sources in the boundary layer from tall tower profiles of water vapor and
769   surface water isotope ratios after a snowstorm in Colorado, Atmos. Chem. Phys., 13(3), 1607–
770   1623, doi:10.5194/acp-13-1607-2013, 2013.

771   Pfahl, S. and Wernli, H.: Air parcel trajectory analysis of stable isotopes in water vapor in the
772   eastern Mediterranean, J. Geophys. Res. Atmos., 113(D20), n/a–n/a, doi:10.1029/2008JD009839,
773   2008.

774   Pfahl, S. and Wernli, H.: Lagrangian simulations of stable isotopes in water vapor: An evaluation
775   of nonequilibrium fractionation in the Craig-Gordon model, J. Geophys. Res. Atmos., 114(D20),
776   D20108, doi:10.1029/2009JD012054, 2009.

777   Risi, C., Noone, D., Frankenberg, C. and Worden, J.: Role of continental recycling in intraseasonal
778   variations of continental moisture as deduced from model simulations and water vapor isotopic
779   measurements, Water Resour. Res., 49(7), 4136–4156, doi:10.1002/wrcr.20312, 2013.

780   Samuels-Crow, K. E., Galewsky, J., Sharp, Z. D. and Dennis, K. J.: Deuterium-excess in
781   subtropical free troposphere water vapor: continuous measurements from the Chajnantor Plateau,
782   northern Chile, Geophys. Res. Lett., 2014GL062302, doi:10.1002/2014GL062302, 2014.

783   Simonin, K. A., Link, P., Rempe, D., Miller, S., Oshun, J., Bode, C., Dietrich, W. E., Fung, I. and
784   Dawson, T. E.: Vegetation induced changes in the stable isotope composition of near surface
785   humidity, Ecohydrology, 7(3), 936–949, doi:10.1002/eco.1420, 2014.

786   Steen-Larsen, H. C., Johnsen, S. J., Masson-Delmotte, V., Stenni, B., Risi, C., Sodemann, H.,
787   Balslev-Clausen, D., Blunier, T., Dahl-Jensen, D., Ellehøj, M. D., Falourd, S., Grindsted, A.,
788   Gkinis, V., Jouzel, J., Popp, T., Sheldon, S., Simonsen, S. B., Sjolte, J., Steffensen, J. P., Sperlich,
789   P., Sveinbjörnsdóttir, A. E., Vinther, B. M. and White, J. W. C.: Continuous monitoring of summer
790   surface water vapor isotopic composition above the Greenland Ice Sheet, Atmos. Chem. Phys.,
791   13(9), 4815–4828, doi:10.5194/acp-13-4815-2013, 2013.

792   Steen-Larsen, H. C., Sveinbjörnsdottir, A. E., Jonsson, T., Ritter, F., Bonne, J.-L., Masson-
793   Delmotte, V., Sodemann, H., Blunier, T., Dahl-Jensen, D. and Vinther, B. M.: Moisture sources

794 and synoptic to seasonal variability of North Atlantic water vapor isotopic composition, J.
795 Geophys. Res. Atmos., 120(12), 2015JD023234, doi:10.1002/2015JD023234, 2015.

796 Steen-Larsen, H. C., Sveinbjörnsdottir, A. E., Peters, A. J., Masson-Delmotte, V., Guishard, M.
797 P., Hsiao, G., Jouzel, J., Noone, D., Warren, J. K. and White, J. W. C.: Climatic controls on water
798 vapor deuterium excess in the marine boundary layer of the North Atlantic based on 500 days of
799 in situ, continuous measurements, Atmos. Chem. Phys., 14(15), 7741–7756, doi:10.5194/acp-14-
800 7741-2014, 2014.

801 Tian, L., Masson-Delmotte, V., Stievenard, M., Yao, T. and Jouzel, J.: Tibetan Plateau summer
802 monsoon northward extent revealed by measurements of water stable isotopes, J. Geophys. Res.
803 Atmos., 106(D22), 28081–28088, doi:10.1029/2001JD900186, 2001.

804 Uemura, R., Matsui, Y., Yoshimura, K., Motoyama, H. and Yoshida, N.: Evidence of deuterium
805 excess in water vapor as an indicator of ocean surface conditions, J. Geophys. Res. Atmos.,
806 113(D19), n/a–n/a, doi:10.1029/2008JD010209, 2008.

807 Vallet-Coulomb, C., Gasse, F. and Sonzogni, C.: Seasonal evolution of the isotopic composition
808 of atmospheric water vapour above a tropical lake: Deuterium excess and implication for water
809 recycling, Geochim. Cosmochim. Acta, 72(19), 4661–4674, doi:10.1016/j.gca.2008.06.025, 2008.

810 Wang, L., Niu, S., Good, S. P., Soderberg, K., McCabe, M. F., Sherry, R. A., Luo, Y., Zhou, X.,
811 Xia, J. and Caylor, K. K.: The effect of warming on grassland evapotranspiration partitioning using
812 laser-based isotope monitoring techniques, Geochim. Cosmochim. Acta, 111, 28–38,
813 doi:10.1016/j.gca.2012.12.047, 2013a.

814 Wang, L., Niu, S., Good, S. P., Soderberg, K., McCabe, M. F., Sherry, R. A., Luo, Y., Zhou, X.,
815 Xia, J. and Caylor, K. K.: The effect of warming on grassland evapotranspiration partitioning using
816 laser-based isotope monitoring techniques, Geochim. Cosmochim. Acta, 111, 28–38,
817 doi:http://dx.doi.org/10.1016/j.gca.2012.12.047, 2013b.

818 Wei, J., Dirmeyer, P. A., Wisser, D., Bosilovich, M. G. and Mocko, D. M.: Where Does the
819 Irrigation Water Go? An Estimate of the Contribution of Irrigation to Precipitation Using MERRA,
820 J. Hydrometeorol., 14(1), 275–289, doi:10.1175/JHM-D-12-079.1, 2012.

821 Welp, L. R., Lee, X., Griffis, T. J., Wen, X.-F., Xiao, W., Li, S., Sun, X., Hu, Z., Val Martin, M.
822 and Huang, J.: A meta-analysis of water vapor deuterium-excess in the midlatitude atmospheric
823 surface layer, Global Biogeochem. Cycles, 26(3), GB3021, doi:10.1029/2011GB004246, 2012.

824 Williams, A. G., Chambers, S. and Griffiths, A.: Bulk Mixing and Decoupling of the Nocturnal
825 Stable Boundary Layer Characterized Using a Ubiquitous Natural Tracer, Boundary-Layer
826 Meteorol., 149(3), 381–402, doi:10.1007/s10546-013-9849-3, 2013.

827 Williams, A. G., Zahorowski, W., Chambers, S., Griffiths, A., Hacker, J. M., Element, A. and
828 Werczynski, S.: The Vertical Distribution of Radon in Clear and Cloudy Daytime Terrestrial
829 Boundary Layers, J. Atmos. Sci., 68(1), 155–174, doi:10.1175/2010JAS3576.1, 2010.

830 Xu, X., Werner, M., Butzin, M. and Lohmann, G.: Water isotope variations in the global ocean
831 model MPI-OM, Geosci. Model Dev., 5(3), 809–818, doi:10.5194/gmd-5-809-2012, 2012.

832 Zahorowski, W., Chambers, S. D. and Henderson-Sellers, A.: Ground based radon-222
833 observations and their application to atmospheric studies, J. Environ. Radioact., 76(1–2), 3–33,
834 doi:http://dx.doi.org/10.1016/j.jenvrad.2004.03.033, 2004.

835 Zhao, L., Wang, L., Liu, X., Xiao, H., Ruan, Y. and Zhou, M.: The patterns and implications of
836 diurnal variations in the d-excess of plant water, shallow soil water and air moisture, Hydrol. Earth
837 Syst. Sci., 18(10), 4129–4151, doi:10.5194/hess-18-4129-2014, 2014.
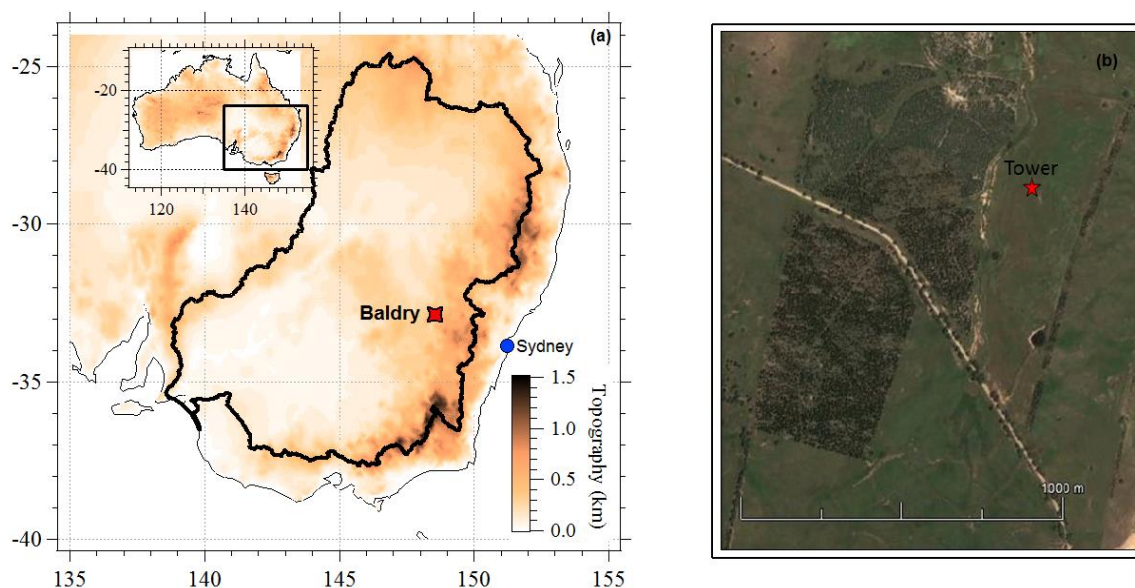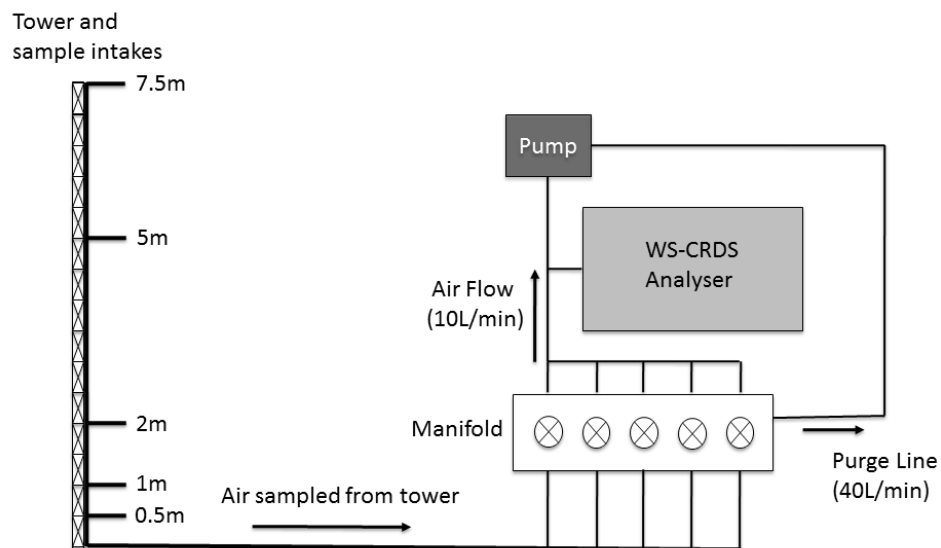
838 **8   Figure Captions**

839

Figure 1: a) Location of the Baldry Hydrological Observatory, with the heavy black border outlining the extent of the Murray-Darling Basin, (b) location of the field site used for the campaign, illustrating the semi-arid grassland and adjacent reforested site.

840

841

842

Figure 2: Sampling system for the automated in-situ collection and measurement of water vapour isotopes from the tower.

845
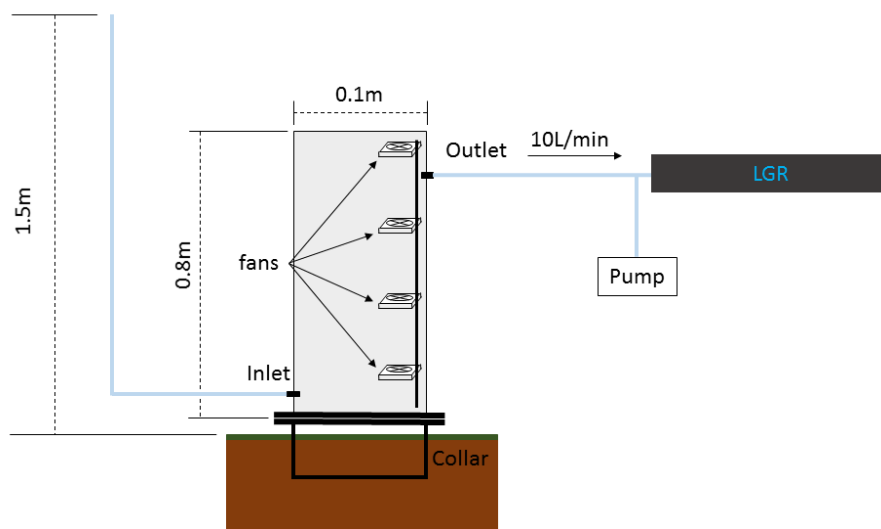
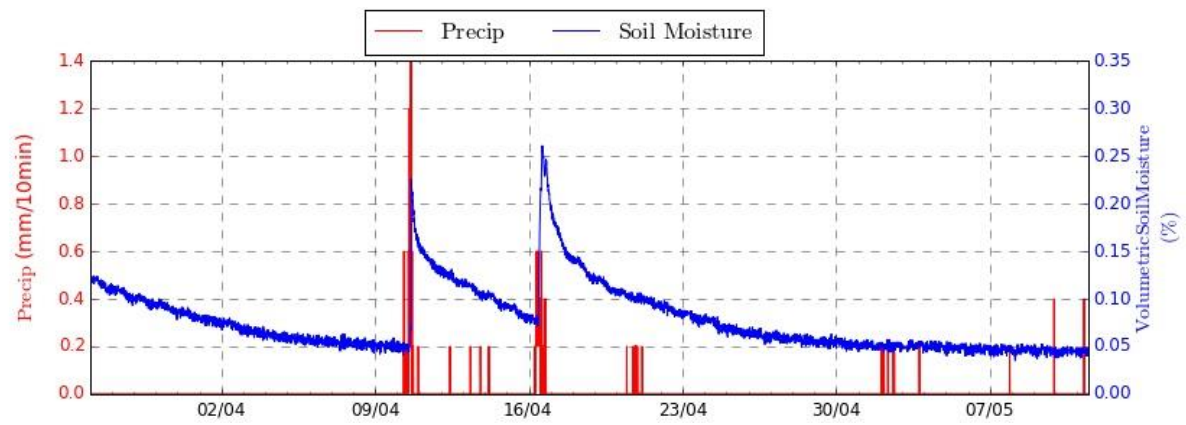Figure 3: Chamber design used for determining the isotopic compositions of ET fluxes.

847

848   Figure 4: Precipitation and 0-10 cm soil moisture for the month leading up to and including the
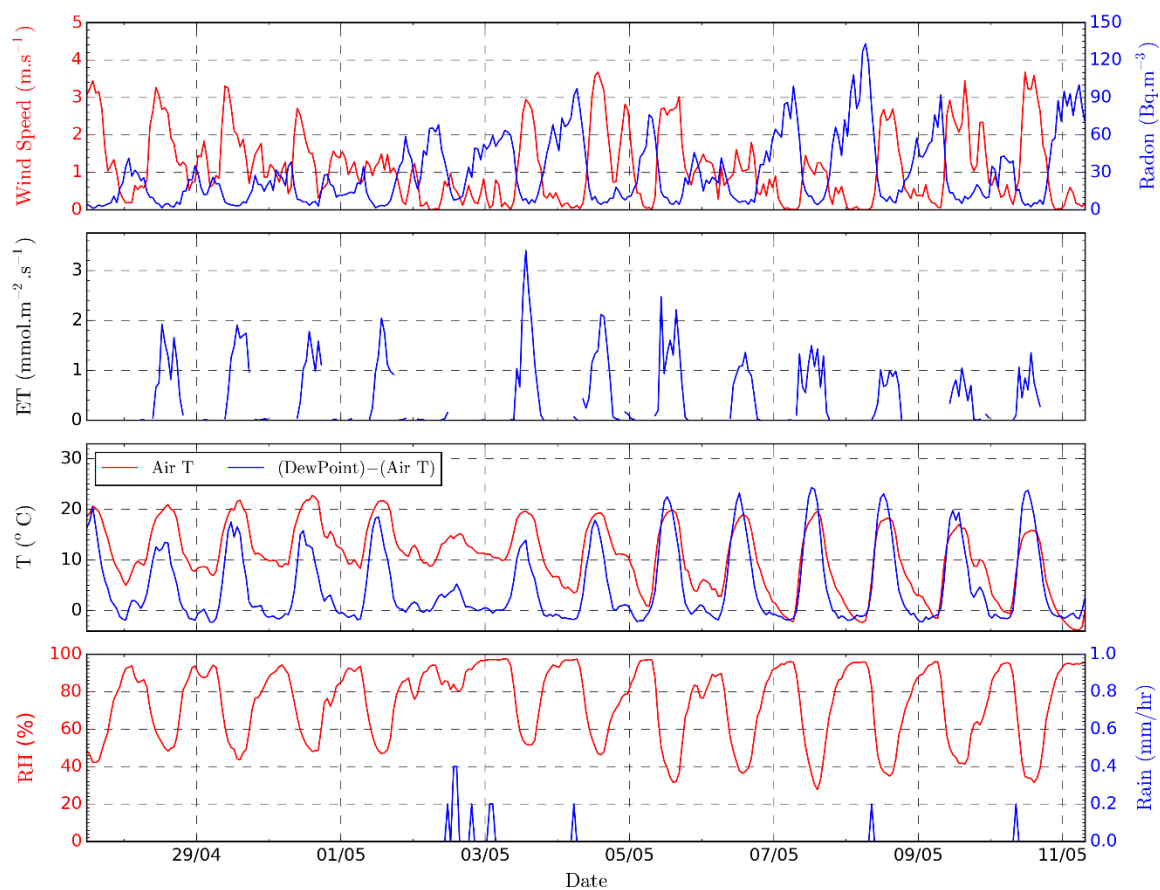849   field campaign.
850

851

Figure 5: Meteorological and radon measurements collected throughout the field campaign. Meteorological measurements are block hourly averages calculated from 15-minute observations. Small rain events on the 4th, 8th and 10th May were most likely dew fall rather than precipitation.
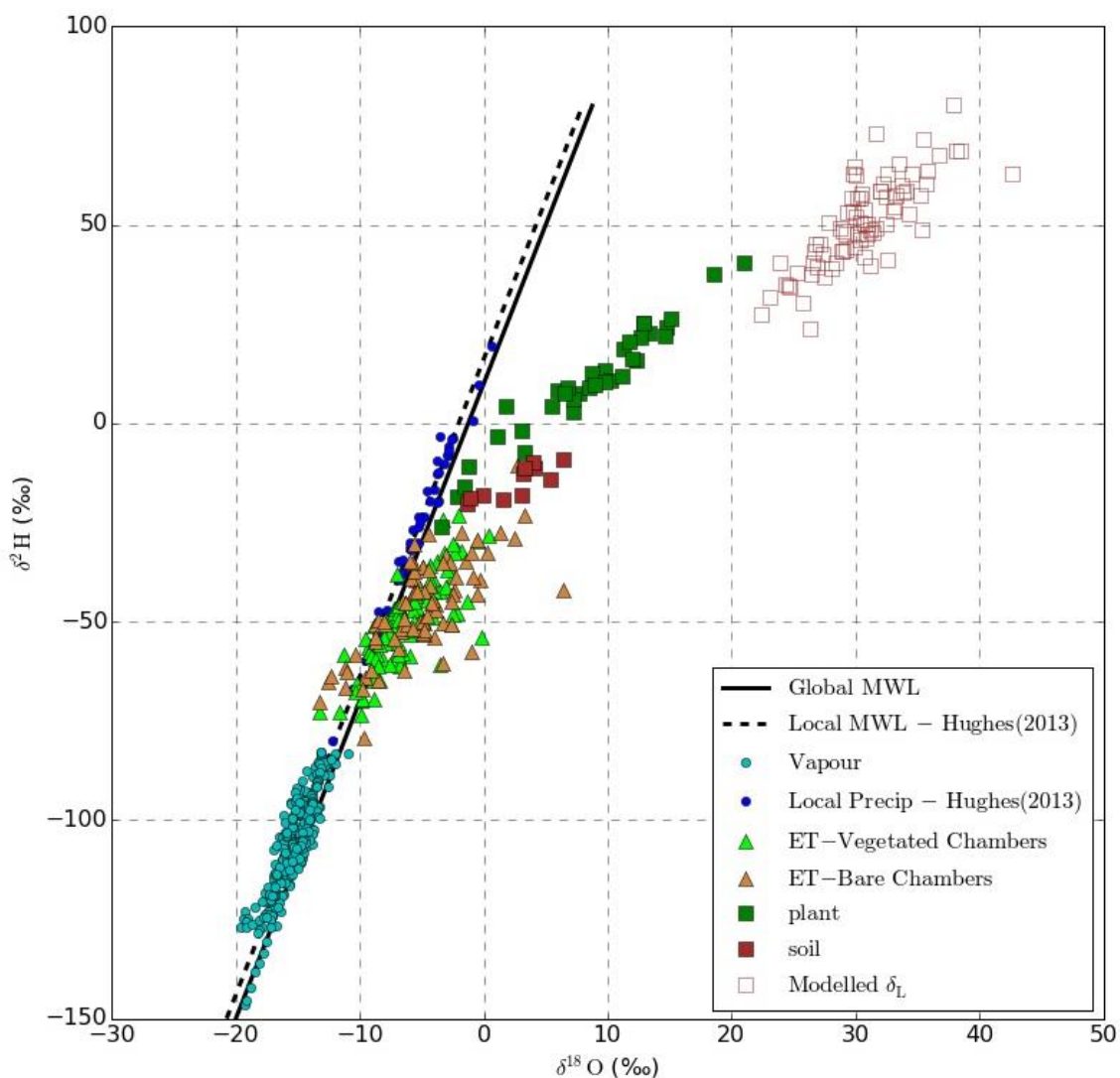
852

853

Figure 6: Relationship between δ^2H and δ^{18}O for observed and modelled water pools. Linear regressions are shown for local and global meteoric water lines (MWL). Data from Hughes and Crawford (2013) are for monthly cumulative rainfall samples between 2005 and 2008.
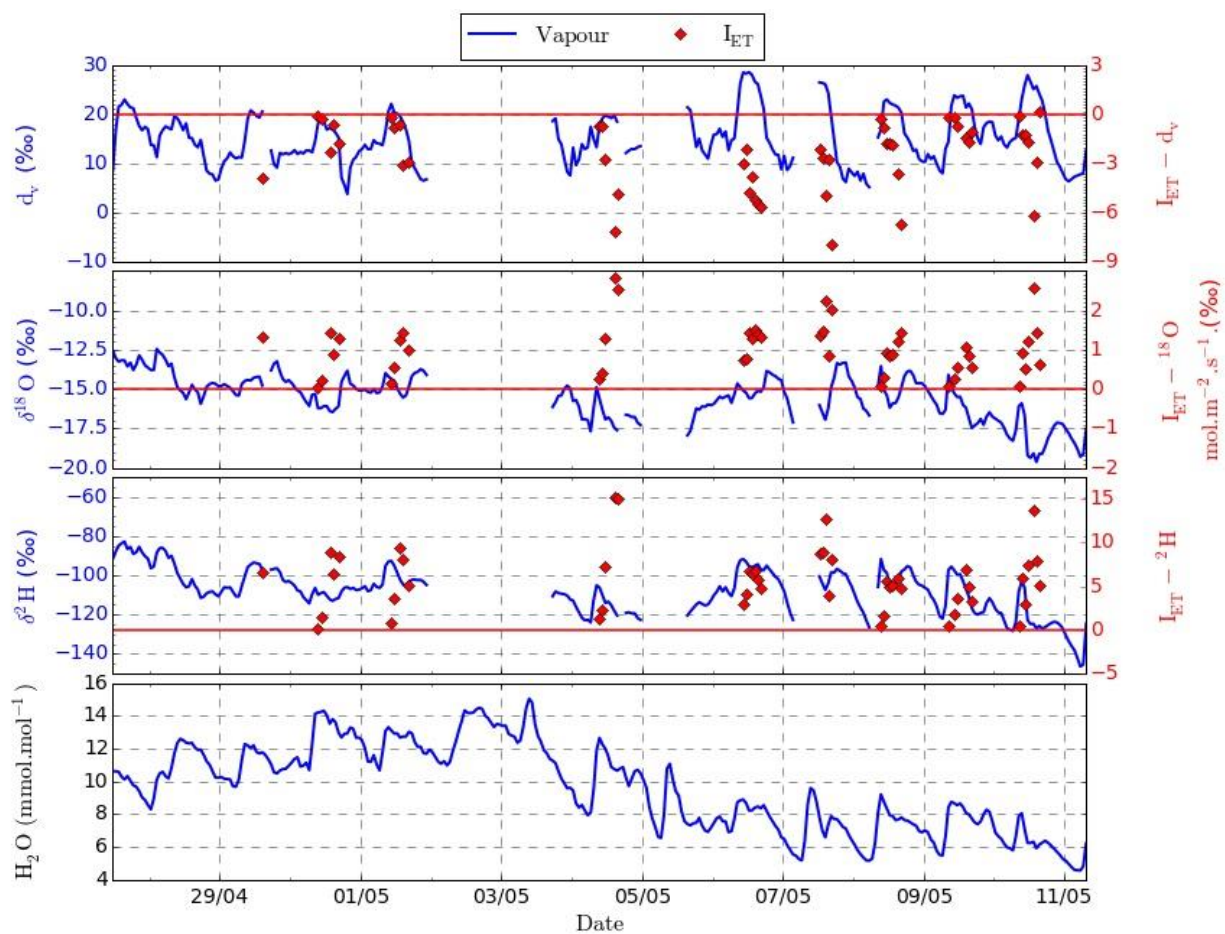
854

855

Figure 7: Time series of hourly water vapour mixing ratio, isotopic composition and ET iso-forcing (I$_{ET}$).
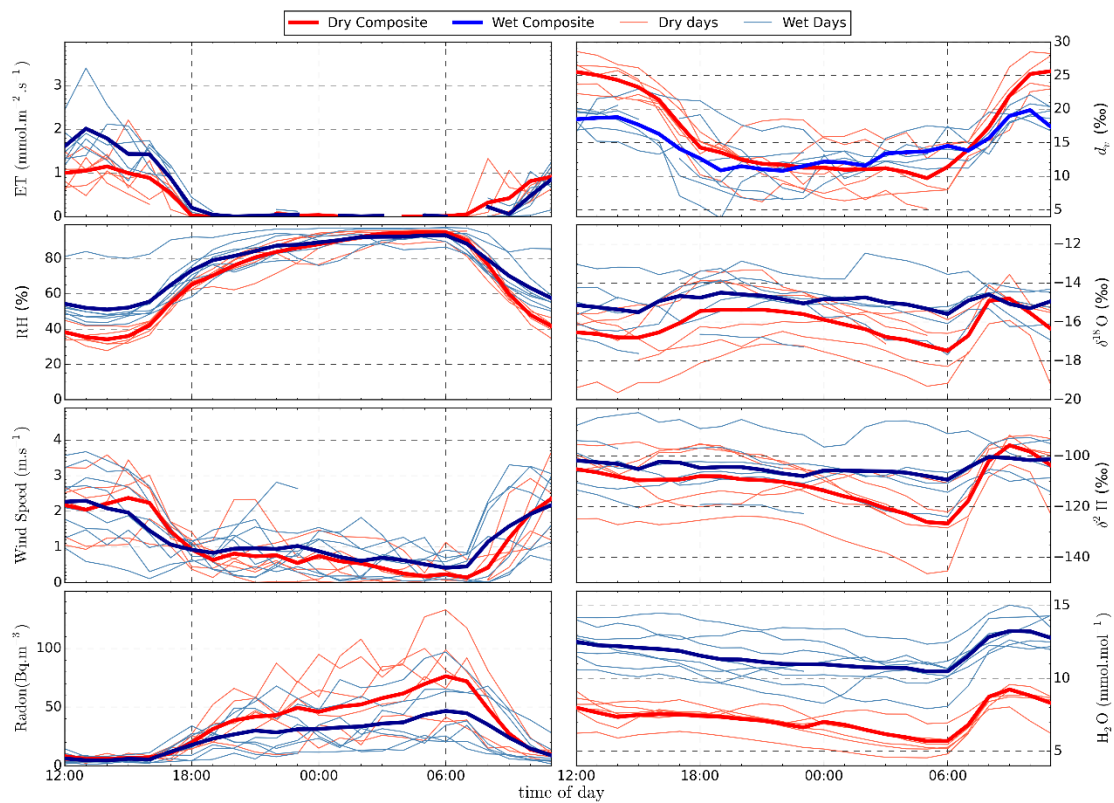
856

857

Figure 8: Data plotted by time of day and divided into dry and wet periods (see text in section 3.5). Diurnal composites are shown for dry (red) and wet (blue) periods.

858

859　Table 1: Correlation between meteorological variables and the isotopic composition of water
860　vapour. Values outside the brackets are statistics for the hourly observations. Inside the brackets
861　are correlation statistics for average values calculated between 11:00 and 15:00 LST, hence
862　representing activity during a convective boundary layer. Significant correlation are shown in bold;
863　p<0.001 for hourly observations and p<0.05 for the daytime averages (due to the smaller number
864　of points).

		T	RH	ET	H_2O	I_{ET}[a]
δ^2H	Slope	**0.83** (0.51)	**-0.17** (0.23)	1.4 (6.1)	**2.1** (0.85)	-1.1 **(-3.0)**
	Intercept	**-120** (-140)	**-95** (-110)	-110 (-110)	**-110** (-130)	-99 **(-83)**
	R^2	**0.24** (0.13)	**0.09** (0.02)	0.001 (0.04)	**0.2** (0.04)	0.2 **(0.45)**
	p	**<0.001** (0.3)	**<0.001** (0.7)	0.32 (0.6)	**<0.001** (0.5)	0.002 **(0.05)**
$\delta^{18}O$	Slope	**0.046** (0.44)	-0.01 (-0.01)	-0.37 (1.8)	**0.27** (0.29)	-0.7 (-1.9)
	Intercept	**-16** (-24)	-16 (-20)	-15 (-18)	**-18** (-19)	-15 (-14)
	R^2	**0.04** (0.30)	0.004 (0.2)	0.02 (0.16)	**0.2** (0.2)	0.14 (0.32)
	p	**<0.001** (0.08)	0.26 (0.19)	0.05 (0.26)	**<0.001** (0.15)	0.008 (0.11)
d_v	Slope	**0.51 (-1.4)**	**-0.21 (-0.52)**	0.01 **(-0.16)**	0.15 **(-1.3)**	-1.4 (-2.4)
	Intercept	**-9.9 (48)**	**31 (44)**	-15 **(-18)**	14 **(35)**	21 (20)
	R^2	**0.40 (0.48)**	**0.62 (0.74)**	0.22 **(0.30)**	0.004 **(0.71)**	0.06 (0.08)
	p	**<0.001 (0.02)**	**<0.001 (<0.01)**	0.05 **(0.01)**	0.26 **(<0.01)**	0.01 (0.44)

865　[a]Iso-forcing correlations were calculated for simultaneous vapour and chamber measurements.
866　Hourly averaged values were used for both.

867